

Sub-Picomolar Detection of SARS-CoV-2 RBD via Computationally-Optimized Peptide Beacons

by

Soumya Pratap Tripathy

Submitted to the Program in Media Arts and Sciences
in partial fulfillment of the requirements for the degree of

Master of Science in Media Arts and Sciences

at the

MASSACHUSETTS INSTITUTE OF TECHNOLOGY

September 2021

© Massachusetts Institute of Technology 2021. All rights reserved.

Author
Program in Media Arts and Sciences
August 20, 2021

Certified by
Joseph M. Jacobson
Associate Professor of Media Arts and Sciences
Thesis Supervisor

Accepted by
Tod Machover
Academic Head, Program in Media Arts and Sciences

Sub-Picomolar Detection of SARS-CoV-2 RBD via Computationally-Optimized Peptide Beacons

by

Soumya Pratap Tripathy

Submitted to the Program in Media Arts and Sciences
on August 20, 2021, in partial fulfillment of the
requirements for the degree of
Master of Science in Media Arts and Sciences

Abstract

The novel coronavirus SARS-CoV-2 continues to pose a significant global health threat. Along with vaccines and targeted therapeutics, there is a critical need for rapid diagnostic solutions. In this work, we employ a deep learning-based protein design to engineer molecular beacons that function as conformational switches for high sensitivity detection of the SARS-CoV-2 spike protein receptor-binding domain (S-RBD). The beacons contain two peptides, together forming a heterodimer, and a binding ligand between them to detect the presence of S-RBD. In the absence of S-RBD (OFF), the peptide beacons adopt a closed conformation that opens when bound to the S-RBD and produces a fluorescence signal (ON), utilizing a fluorophore-quencher pair at the two ends of the heterodimer stems. Two candidate beacons, C17LC21, and C21LC21 can detect the S-RBD with limits of detection (LoD) in the sub-picomolar range. We envision that these beacons can be easily integrated with on-chip optical sensors to construct a point-of-care diagnostic platform for SARS-CoV-2.

Thesis Supervisor: Joseph M. Jacobson

Title: Associate Professor of Media Arts and Sciences

Sub-Picomolar Detection of SARS-CoV-2 RBD via Computationally-Optimized Peptide Beacons

by

Soumya Pratap Tripathy

This thesis has been reviewed and approved by following committee
members:

Joseph M. Jacobson
Associate Professor of Media Arts and Sciences
Massachusetts Institute of Technology

Edward S. Boyden
Professor of Media Arts and Sciences
Massachusetts Institute of Technology

Joseph A. Paradiso
Professor of Media Arts and Sciences
Massachusetts Institute of Technology

Acknowledgments

This thesis would not have been possible without the support and assistance of many people.

First and foremost, I would like to thank my advisor, Dr. Joseph Jacobson, for guiding and supporting me over the years. And for providing a space for independent thoughts.

I would like to thank Dr. Pranam Chatterjee and Manvitha Ponnampati for assisting me in the computational design and optimisation. My thesis would not be possible without their guidance and help. I would also like to thank other members of the molecular machines group - Eyal, Ruihan and Allan for the support and friendship.

I extend my gratitude towards my beloved parents for their tremendous support and love. I want to thank my friend Somesh Mohapatra for his positivity and friendship.

Contents

1		15
1.1	Introduction	15
1.2	Overview	16
2	Detection of SARS-CoV-2 RBD via Peptide Beacons	17
2.1	Engineering of Peptide Beacon Architecture	17
2.2	Computational Selection of Peptide Beacon Candidates	18
2.3	Validation of S-RBD Binding in Human Cells	18
2.4	<i>In vitro</i> Detection of S-RBD	19
2.5	Discussion	20
2.6	Materials and Methods	20
2.6.1	<i>In silico</i> Selection of Candidate Peptide Beacons	20
2.6.2	Generation of Plasmids	21
2.6.3	Cell Culture	21
2.6.4	Peptide Synthesis and Purification	22
2.6.5	<i>In vitro</i> Detection of S-RBD	22
2.6.6	Statistics and Reproducibility	23
3	Fabrication of miniaturized TIRF based fluorescence sensor	25
3.1	Design of the mini-TIRF	25
3.2	Confirmation of the presence of evanescent wave on mini-TIRF	28
3.3	Detection of Biotin-FITC using mini-TIRF	29
3.4	Discussion	29

3.5	Materials and Methods	30
3.5.1	Fabrication of Device	30
3.5.2	Performance of Device	31
3.5.3	Statistics and Reproducibility	31
A	Figures	33

List of Figures

A-1	Engineering of peptide beacon architecture. A) Low-fluorescent state is the closed heterodimer state of the peptide beacon in the absence of S-RBD. B) High-fluorescent state is the open-coil state after binding of S-RBD with the loop of the peptide beacon. C) CxxL (25 uM, 1X PBS, pH 7.4) was added to C21 (25 uM, 1X PBS, pH 7.4) and incubated at room temperature for 2 hours for the conjugation reaction between the thiol groups of cysteine at the N-terminus of CxxL and the maleimide on the N-terminus of C21.	33
A-2	<i>In silico</i> verification of peptide beacon architecture. A) Validation pipeline. Sequences were folded ab initio via trRosetta or Rosetta Abinitio. The top structures were docked to S-RBD via HDOCK. Docked structures were analyzed and candidate beacons were chosen. Highest scoring B) trRosetta structures C) Rosetta Abinitio structures and D) Docked HDOCK structures of the three candidate beacons. The conserved binding peptide moiety is highlighted in orange. S-RBD (derived from PDB 6MOJ) is indicated in blue.	34

A-3 Experimental characterization of peptide beacons. A) Analysis of S-RBD-sfGFP degradation by flow cytometry. All samples were performed in independent transfection duplicates (n=2) and gated on GFP+ fluorescence. Mean percentage of GFP+ cell depletion was calculated in comparison to the S-RBD-sfGFP only control. C13LC21 is referred to as C13-A2N-C21*, C17LC21 is referred to as C17-A2N-C21*, and C21LC21 is referred to as C21-A2N-C21*. Titration of the target recombinant S-RBD and Influenza H3N2 (HA) with 2 nM of HPLC-purified B) C13LC21 (n=3), C) C17LC21 (n=5), D) C21LC21 (n=3) in 1X PBS, pH 7.4. 35

A-4 Purification and synthesis of peptide beacons. A-C) MALDI-TOF mass spectrum of CxxL+C21 shows peaks corresponding to C21, CxxL, and CxxLC21. D-F) HPLC chromatograms of CxxLC21, plotted with HPLC chromatograms of CxxL and C21. The chromatogram of C13L+C21, C17L+C21, and C21L+C21 shows the appearance of new peaks having retention times of 38 min, 37 min, and 36 min, respectively (new peaks marked in colored dot in D-E). Fraction of material corresponding to new peaks was collected during HPLC. G-I) MALDI-TOF mass spectrum of collected fraction from HPLC of CxxL+C21 shows dominant peak corresponding to CxxLC21 and negligible peaks corresponding to CxxL and C21. CxxL+C21 represents the reaction mixture of CxxL and C21 after 2 hours of reaction at room temperature. CxxLC21 represents the peptide beacons. 36

A-5	Design of the mini-TIRF based evanescent-wave fluorescence sensor. The collimated LASER beam hits the side surface of the waveguide at an angle such that the refracted beam within the glass core will hit the core-cladding interface at an angle more than the critical angle of the core-cladding pair. Subsequently, the LASER beam propagates along the length of the waveguide bouncing between the top and bottom core-cladding interface. An optical setup consisting of lens-bandpass filter-SiPM is used to detect the fluorescence emission. The fluorescence signal is quantified through ADC after amplification of the SiPM signal. The top view shows the TIR spots where the laser beam hits the core-cladding interface and creates evanescent waves. L_{TIR} and W_{TIR} are the dimensions of the TIR spot along the length and width of the waveguide.	37
A-6	Design of cartridge. A. 3D printed cartridge. B. The LASER diode (LD) housing holds the LD and collimates the LASER beam. The LD housing is placed at a coupling angle of 38° with the plane of the waveguide. The sample well is parallel and aligned with the lens, filter, and SiPM. C. The graph between angle of incidence that allows TIR and corresponding coupling angles. D. Penetration depths of evanescent field at a different angle of incidence at the core-cladding interface. E. Overlap between bandpass spectrum of the optical filter and emission spectrum of FITC excited at 488 nm.	38
A-7	Confirmation of the presence of evanescent field on mini-TIRF. Z-stack imaging of fluorescent microspheres ($1\ \mu\text{m}$) deposited on the glass core within the sample well under A) TIR and B) epi-illumination at $1\ \mu\text{m}$ step from surface to $50\ \mu\text{m}$ above the surface. C. Focal plane at $50\ \mu\text{m}$ above the surface under TIR illumination. D. Focal plane at $50\ \mu\text{m}$ above the surface under epi-illumination. E. Focal plane at the surface ($z=0\ \mu\text{m}$) under TIR illumination. F. Focal plane at the surface ($z=0\ \mu\text{m}$) under epi-illumination.	39

- A-8 Fabricated device. A. White box contains the amplification module and Teensy 3.6 development board, along with slots for battery intended for biasing the amplification module. On the top surface of the white box, there are slots for LD pins and SiPM pins. B. LD pins and SiPM pins on the bottom of the cartridge go to the slots on the top surface of the white box. C. The cartridge firmly sits on the box after the LD pins and SiPM pins entering the respective pin slots. D. The lid covers the SiPM to provide a light-tight environment during signal acquisition. 40
- A-9 Detection of biotinylated FITC using mini-TIRF. A. Schematic showing the excitation of biotinylated FITC bound to surface immobilized streptavidin by evanescent field. Bandpass filter selectively allows fluorescent emission and stops stray photons from the scattered evanescent field caused by surface-bound molecules. SiPM detects the photons from the fluorescence emission and an ADC of a microcontroller detects the SiPM signal after amplification. B. Detection of biotinylated FITC in 1X PBS, pH 7.4 from attomolar to micromolar concentration using mini-TIRF. The LoD is defined as the signal more than the baseline signal by thrice of the standard deviation of the baseline signal. 41

Chapter 1

1.1 Introduction

As numerous countries are experiencing additional waves of COVID-19, rapid, point-of-care diagnostic tests enable triage of symptomatic individuals and control the outbreaks of the disease. The most widely employed diagnostic tests for SARS-CoV-2 are reverse transcription-polymerase chain reaction (RT-PCR)-based methods [28], though other technologies based on CRISPR and loop-mediated amplification have been deployed as well [22, 11, 5, 18]. The best-in-class FDA authorized diagnostics, such as RT-PCR, have limits of detection (LoD) of 10^2 - 10^3 RNA copies/ml, which is about 1-10 attomolar (aM) RNA in the test volume [16]. RT-PCR tests, however, require laborious and expensive nucleic acid isolation, purification, and processing steps, which increases both the turnaround time of detection and the cost of testing [16, 6]. Alternatively, there are FDA-authorized low-sensitivity, inexpensive, and rapid diagnostics. These tests, which often rely on antigen detection, have LoDs of 10^5 - 10^7 RNA copies/ml, or around 1-100 femtomolar (fM)[9].

Recently, there has been significant effort to detect SARS-CoV-2 via fluorescence-based readouts to allow for specific signal amplification [3, 32, 10, 15]. Such methods largely rely on binding to SARS-CoV-2 RNA or DNA, which requires isolation of nucleic acids, as described above. In this study, we develop a molecular assay to detect the spike protein receptor-binding domain (S-RBD) of SARS-CoV-2 using computationally validated peptide beacons, which enable single-step detection of S-RBD

presence through the production of a fluorescence signal. Our eventual goal is to integrate these optimized beacons within miniaturized total internal reflection fluorescence (mini-TIRF) microscopes, which provide exquisite sensitivity by exciting fluorophores present within nanometer proximity of the device surface [29], producing high signal-to-background ratios and enabling rapid and ultra-sensitive detection of SARS-CoV-2.

1.2 Overview

Chapter 2 discusses the design, synthesis, and characterization of molecular beacons that can detect S-RBD. Chapter 3 discusses the design, fabrication, and performance of the mini-TIR: an attomolar-sensitive evanescent wave fluorescence sensor.

Chapter 2

Detection of SARS-CoV-2 RBD via Peptide Beacons

2.1 Engineering of Peptide Beacon Architecture

Our molecular beacon design includes two heterodimer-forming peptides, a binding ligand to the S-RBD, as well as a fluorophore-quencher pair at the terminal ends of the beacon (Figure A-1A). This fluorophore-quencher pair induces fluorescence quenching through the mechanism of Förster resonance energy transfer (FRET), where the efficiency of energy transfer between the fluorophore and quencher is proportional to their spatial distance. Hence, a small change in spatial distance between the two beacon arms can drastically change the FRET efficiency, thus affecting the fluorescent quantum yield of the fluorophore. Here, we utilized a commonly-used fluorophore-quencher pair: fluorescein isothiocyanate (FITC) and 4-(dimethylaminoazo)benzene-4-carboxylic acid (DABCYL), respectively. Upon binding to the target protein, the fluorophore and quencher are separated enough to observe an increase in fluorescence signal proportional to the amount of S-RBD present (Figure A-1B).

2.2 Computational Selection of Peptide Beacon Candidates

We utilized the coiled-coil peptide beacons designed by Mueller, et al. [20]. Mueller, et al., employed the parallel heterodimer reported by Thomas, et al., to design acidic 21mer peptide portions of a beacon detecting CREB binding protein [26]. The reported peptide beacon designs consisted of the 21mer conjugated with a binding ligand and one of the three basic peptides: C13, C17, C21 [20]. We designed our peptide beacons by replacing the binding portion of the sequences designed by Grossman with our previously engineered 23mer peptide that can bind to S-RBD and induce its degradation via the ubiquitin-proteasomal pathway [8].

To computationally verify that insertion of our 23mer peptide confers S-RBD binding capability to our peptide beacon sequences, we folded and docked the three designs (C13LC21, C17LC21, C21L21) using trRosetta, Rosetta, and HDOCK (Figure A-2A) [34, 4, 33]. Our results show that in the absence of S-RBD, all three peptides show terminal ends of the beacons, representing the fluorophore and the quencher, in close proximity to each other (OFF) in at least one of the top predicted models from trRosetta [34] or Rosetta Abinitio [4] (Figure 2B-2C). Alternatively, when the peptide beacon sequences were docked against S-RBD utilizing HDOCK [33], we observed the terminal ends to be spatially distanced from each other, indicating a possible ON state (Figure A-2D). These results motivated us to test these three peptide beacon designs experimentally.

2.3 Validation of S-RBD Binding in Human Cells

To rapidly validate the binding capability of our peptide beacon designs, we adapted our previously-described degradation assay in human cells, by fusing our peptide beacon candidates to the CHIP Δ TPR E3 ubiquitin ligase, which can tag target proteins for degradation via the ubiquitin-proteasomal pathway in human cells. [8]. After

co-transfection with a plasmid expressing S-RBD C-terminally fused to superfolder GFP (sfGFP), we can measure binding affinity to S-RBD as relative to sfGFP degradation. We tested various peptide beacon combinations, employing our validated mutant S-RBD-binding peptide derived from ACE2, A2N [8], as well as a positive nanobody control, which has shown high affinity to S-RBD [31]. As expected, these moieties alone demonstrate robust degradation capabilities, while the arms-only negative controls (C13, C17, C21, and C21*) show negligible degradation, hence no binding to the S-RBD. Of the complete peptide beacon constructs, the C17-A2N-C21* (C17LC21) beacon induces the greatest level of degradation of S-RBD-sfGFP, followed by C21LC21 and C13LC21, the latter of which exhibited minimal degradation capabilities (Figure A-3A).

2.4 *In vitro* Detection of S-RBD

After ascertaining the binding capability of our candidates in human cells, we characterized the response of the peptide beacons *in vitro* in the presence of S-RBD. As a negative control, we also measured the cross-reactivity of our peptide beacons towards the Hemagglutinin protein of Influenza A H3N2 (HA) [24]. We first purified peptide beacons (CxxLC21) from the reaction mixture of CxxL+C21, using high-performance liquid chromatography (HPLC), and confirmed the presence of CxxLC21 in the collected fraction from HPLC through MALDI-TOF mass spectrometry (Supplementary Figure 1). We measured the fluorescent signals from the peptide beacons following a 10-minute exposure to different concentrations of S-RBD and HA in 1X PBS and pH 7.4 (Figure 3B-D). Of the three peptide beacons, C17LC21 showed highest sensitivity towards S-RBD with a LoD of nearly 20 fM ($K_d = 1.615 \times 10^{-12}$), followed by C21LC21 having an LoD of 400 fM ($K_d = 6.766 \times 10^{-13}$). However, C13LC21 showed negligible response towards both S-RBD and HA. In conclusion, C17LC21 and C21LC21 can detect the presence of S-RBD with sub-picomolar sensitivity and low cross-reactivity, thus motivating their application for rapid detection of SARS-CoV-2.

2.5 Discussion

In this study, using existing deep learning tools for protein structure prediction and energy-based modeling suites, we designed and tested a set of molecular beacons that can potentially bind to the S-RBD and release a fluorescence signal via FRET, enabling sub-picomolar detection levels. Integration of these peptide beacons within optical sensors, such as miniature TIRF microscopes, may reduce the LoD to sub-femtomolar level, thus yielding a rapid, point-of-care diagnostic platform for SARS-CoV-2. Such a diagnostic would be faster than existing RT-PCR assays and more sensitive than antigen-based rapid testing.

Our pipeline also showcases a use case for current deep learning tools for protein structure prediction in a protein design pipeline. Using this approach, molecular beacons can be designed to detect protein targets within other viral species. In addition, by using existing protein structure prediction tools to get rapid insights into the structure of the protein, it may be possible to design an entire peptide beacon sequence from scratch even in the absence of a known binding partner. By fixing the heterodimer motif, binding loops of molecular beacons can be filled in via protein hallucination, using tools like trRosetta [1]. Thus, by employing a hybrid approach of state-of-the-art protein modeling tools and robust experimental validation, our molecular beacon design pipeline serves as a powerful platform to fight COVID-19 and future emergent viral threats.

2.6 Materials and Methods

2.6.1 *In silico* Selection of Candidate Peptide Beacons

The three peptide beacon sequences were folded in the absence of S-RBD using trRosetta. trRosetta is a deep learning tool to predict structures from sequence information [34]. The three peptide beacon sequences were also folded using Rosetta Abinitio folding. Abinitio folding solves the protein structure from sequence through

physics-based constraints rather than relying on previously solved structures like trRosetta [4]. The three peptide beacon sequences were docked against the S-RBD using HDOCK. HDOCK is a protein-protein docking platform that combines ab-initio docking and template-based modeling [33]. The top 100 predictions from HDOCK were analyzed to visualize the structure of peptide beacon sequences in the presence of S-RBD.

2.6.2 Generation of Plasmids

pcDNA3-SARS-CoV-2-S-RBD-sfGFP (Addgene #141184) and pcDNA3-R4-uAb (Addgene #101800) were obtained as gifts from Erick Procko and Matthew DeLisa, respectively. Peptide beacon sequences were ordered as gBlocks (IDT) and were amplified with overhangs for Gibson Assembly-mediated insertion into linearized pcDNA3-R4-uAb digested with HindIII and EcoRI. Assembled constructs were transformed into 50 μ L NEB Turbo Competent *E. coli* cells, and plated onto LB agar supplemented with the appropriate antibiotic for subsequent sequence verification of colonies and plasmid purification.

2.6.3 Cell Culture

HEK293T cells were maintained in Dulbecco’s Modified Eagle’s Medium (DMEM) supplemented with 100 units/mL penicillin, 100 mg/mL streptomycin, and 10% fetal bovine serum (FBS). RBD-sfGFP (250 ng) and peptide-E3 ligase fusion (250 ng) plasmids were transfected into cells (2×10^5 /well in a 24-well plate) with Lipofectamine 3000 (Invitrogen) in Opti-MEM (Gibco). After 5 days post-transfection, cells were harvested and analyzed on a BD FACSCelesta flow cytometer (BD Biosciences) for GFP fluorescence (488-nm laser excitation, 530/30 filter for detection). Cells expressing GFP were gated, and percent GFP+ depletion to the RBD-sfGFP only control was calculated. All samples were performed in independent transfection duplicates ($n=2$), and percentage depletion values were averaged. Standard deviation was used to calculate error bars.

2.6.4 Peptide Synthesis and Purification

CxxL (25 μ M, 1X PBS, pH 7.4) was added to C21 (25 μ M, 1X PBS, pH 7.4) and incubated at room temperature for 2 hours for the conjugation reaction between the thiol group of Cysteine at the N-terminus of CxxL and the maleimide group at the N-terminus of C21 (Figure A-1C). CxxL+C21 is used to represent the reaction mixture obtained after 2 hours of reaction between CxxL and C21 in 1X PBS, pH 7.4 at room temperature. MALDI-TOF mass spectroscopy of CxxL+C21 confirms the presence of CxxLC21 in CxxL+C21 along with CxxL and C21 (Supplementary Figure 1A-1C). The reaction mixture of CxxL and C21 contains the mixture of individual CxxL, C21, and CxxLC21 after 2 hours of reaction in 1X PBS, pH 7.4 at room temperature. Consequently, CxxLC21 from CxxL+C21 was purified using high-performance liquid chromatography (HPLC) (Agilent 1100) using a C14 H31 column. HPLC chromatogram of CxxL+C21 contains peaks at distinct retention time than that of CxxL and C21 in HPLC chromatogram (Supplementary Figure 1D-1F), which are considered as the fraction containing CxxLC21. The fraction was collected and MALDI-TOF mass spectroscopy was performed (Microflex LRF, Bruker), confirming the presence of CxxLC21 at a higher concentration than that of CxxL and C21 (Figure A-4G-I). The collected fraction was freeze-dried and used for the detection of S-RBD and HA.

2.6.5 *In vitro* Detection of S-RBD

S-RBD (Abcam ab273065) and Influenza H3N2 hemagglutinin (HA) (MyBioSource MBS5308351) were titrated against purified CxxLC21. S-RBD and HA proteins were serially diluted in 1X PBS, pH 7.4 from nanomolar (nM) to attomolar (aM) concentration. 2 nM of CxxLC21 in 1X PBS, pH 7.4 (n=3 or 5) was exposed to different concentrations of the target protein (S-RBD or HA) and incubated for 10 minutes at room temperature. Fluorescence intensity was subsequently measured using a Tecan Spark well plate reader at excitation and emission wavelength of 470 nm and 525 nm, respectively. The fluorescence data were fitted to one site total binding with

saturation curve in the Prism software using the following equation:

$$Y = \frac{Bmax * X}{K_d + X} + NS * X + Background$$

where Y is the fraction of peptide beacon bound to target, $Bmax$ is the maximum binding in units of Y , X is the concentration of target, K_d is the equilibrium dissociation constant in units of X , and NS is the slope of the non-linear regression. The fraction of peptide beacon bound to target (Y) is calculated by normalizing fluorescent intensities obtained at different (X) by considering the highest fluorescence intensity obtained at maximum S-RBD concentration as hundred percent. The limit of detection (LoD) is estimated from the equation given below.

$$LoD = Y_{Blank} + 3 * SD_{Blank}$$

2.6.6 Statistics and Reproducibility

All samples were performed in independent duplicates (n=2), triplicates (n=3), or quintuplicates (n=5), as indicated. Standard deviation was used to calculate error bars. Statistical analyses were performed using the two-tailed Student's t-test, using the GraphPad software package.

Patents of the works from the chapter 2

P.C., M.P., S.P.T, and J.M.J. are listed as inventors for U.S. Provisional Patent Application 63/182,537 entitled "Peptide-Based Probes For the Detection of SARS-CoV-2."

My Contributions

1. Conceptualize and optimized the peptide beacon route for detection of RASRS-CoV-2.
2. Conducted peptide beacon purification, synthesis, and *in vitro* characterization.
3. Conducted data analysis.

Data and Code Availability Statement

All data needed to evaluate the conclusions in the paper are present in the paper at:
<https://doi.org/10.1101/2021.06.04.447114>.

Chapter 3

Fabrication of miniaturized TIRF based fluorescence sensor

3.1 Design of the mini-TIRF

In a total internal reflection fluorescence microscope (TIRF), an evanescent wave excites surface-bound fluorophores and detects fluorescence emission with a high signal-to-noise ratio. The instrumentation of the TIRF microscope primarily involves the production of an evanescent wave through a TIR event at the core-cladding interface, and an image sensor system to image fluorescence emission. TIRF microscope delivers exquisite sensitivity by exciting fluorophores present within nanometer proximity of the device surface [29], producing high signal-to-background ratios. There are several reports on single molecular imaging using TIRF microscope [28, 30, 19, 27, 2, 17, 12, 23], and for single-molecule analysis [7, 14, 35], with an LoD starting from nanomolar (nM) [25], femtomolar (fM) [12] to attomolar (aM) [13] regime. Here, we fabricated a miniaturized version of the TIRF microscope (mini-TIRF) and used a single-photon sensitive silicon photomultiplier (SiPM) photodetector to detect the fluorescence signal from the surface-bound fluorescent molecules excited by the evanescent field.

We used a planar waveguide consisting of glass core ($n=1.53$) and low refractive

index polymer cladding ($n=1.34$) in the mini-TIRF. Generally, a TIR happens when angle of incidence (θ_i) of light is more than the critical angle ($\theta_{critical}$) of the core-cladding interface and produces evanescent field in the cladding within hundreds of nanometer above the surface of the core. The critical angle of the used glass-polymer pair is 61.142° for 488 nm of light which is calculated using following equation:

$$\theta_{critical} = \sin^{-1}\left(\frac{n_{cladding}}{n_{core}}\right) \quad (3.1)$$

Where, $n_{cladding}$ and n_{core} are the refractive index of cladding and the core.

We coupled the laser beam to the side surface of the core, where the collimated laser beam incidents on the side surface of the core at an angle (θ_C) such that the refracted laser beam will hit the core-cladding interface at an angle more than the critical angle of the core-cladding pair (Figure A-5). Thus, the laser beam propagates along the waveguide bouncing between the top and bottom core-cladding interface creating multiple TIRs. We considered a range of angles of incidence greater than the critical angle of the core-cladding interface. Using the below equation we calculated a range of coupling angles corresponding to the above angle of incidence (Figure A-6):

$$\theta_C = \sin^{-1}(n_{core} \sin(\frac{\pi}{2} - \theta_i)) \quad (3.2)$$

The intensity of the evanescent field exponentially decreases above the core surface. Penetration depth is a height from the surface after which the intensity of evanescent wave drops by $1/e$ (37%) [21]. We calculated the penetration depth (d) of the evanescent field for the range of angles of incidence using the below equation (Figure A-6):

$$d = \frac{\lambda_{excitation}}{4\pi \sqrt{n_{core}^2 \sin^2 \theta_i - n_{cladding}^2}} \quad (3.3)$$

Where the $\lambda_{excitation}$ is the wavelength of the excitation source.

TIR spots are the small areas on the core along the line of propagation of the laser beams, where TIR happens within the core and evanescent field penetrates to the cladding (Figure A-5). To use the evanescent field for the excitation of the fluorophore, the fluorescent molecules should bind to the surface of the core within the TIR spot and the photodetector should be placed below or, above the TIR spot to efficiently detect the fluorescent emission. L_{TIR} and W_{TIR} are the dimensions of the TIR spot along the length and width of the waveguide, where W_{TIR} is approximately the same as the width of the laser beam falling on the side surface of the waveguide-3 mm. L_{TIR} is calculated following the below equation:

$$L_{TIR} = \frac{t_{core}}{\tan(\frac{\pi}{2} - \theta_i)} \quad (3.4)$$

We considered a coupling angle of 38 ° which provides a angle of incidence of 66.272° creating a evanescent field with a penetration depth about 88 nm and L_{TIR} of 1.7 mm. The first TIR happens within 1.7 mm from the coupling edge of the waveguide and the subsequent position of the TIR spots are calculated. We coated the glass core with polymer cladding leaving a 3*3 mm^2 area on the core uncoated on the fifth TIR spot. The glass core contains streptavidin coating on the surface, which helps to capture biotinylated molecules on the core surface of the core. Hence, the uncoated area contains streptavidin on its surface so that biotinylated FITC can bind and we can test the performance of the device.

To detect the fluorescence emission, we used a combination of a lens, dichroic filter, and SiPM (Figure A-5). Since we intended to observe the fluorescence emission

from FITC, we used a bandpass optical filter (530 nm, FWHM 24 nm) that specifically allows the fluorescence emission from FITC and stops the photons from the excitation (Figure A-6). Since the fluorescence emission from the device surface is not a collimated beam, a plano-convex lens is used to collimate the fluorescence emission from the surface-bound fluorophores so that the emitted light will hit the lens at 0° of incidence, which is a necessary condition for the dichroic filter to work as intended. Here, a commercially available SiPM evaluation kit is used. The amplified signal from the SiPM is acquired through the analog-to-digital converter (ADC) of a Teensy 3.6 development board at 15-bit resolution with a reference voltage of 3.3 V. The acquired digitized signal was integrated over one second, which quantifies the intensity of light falling on the SiPM.

3.2 Confirmation of the presence of evanescent wave on mini-TIRF

Since the evanescent wave is confined within hundreds of nanometers above the surface, under mini-TIRF illumination, only surface-bound microspheres will be excited and emit fluorescence. However, under the epi-illumination mode, microspheres both on the surface and within the drop will be excited by the laser beam (Figure A-7). Hence, during z-stack imaging, new fluorescent microspheres appeared at subsequent focal planes above the surface under epi-illumination. However, in the case of mini-TIRF illumination, a fixed number of fluorescent microsphere appeared at the focal plane coinciding with the surface of the core, and the fluorescence from the same microspheres faded gradually when the focal plane moves up above the surface, and eventually, the fluorescence will become indistinct (Figure A-7). Furthermore, no new microspheres appeared at subsequent focal planes above the surface under mini-TIRF illumination, thus suggests the mini-TIRF illumination is caused by the evanescent field.

3.3 Detection of Biotin-FITC using mini-TIRF

After ascertaining the presence of an evanescent field on the mini-TIRF, we characterized the performance of the device by measuring the fluorescence of biotinylated FITC. As a baseline, we also measured the fluorescent intensity of 1X PBS and pH 7.4. We measured the fluorescent signals from the biotinylated FITC in 1X PBS and pH 7.4 following a 30-minute exposure to the immobilized streptavidin layer on the surface of the core (Figure A-9A). The mini-TIRF showed a significant increase in signal at 100 aM concentration of biotinylated FITC from the baseline signal. However, biotinylated FITC at concentrations of 1 aM and 10 aM showed a signal not significantly different from the baseline signal. In conclusion, the mini-TIRF can detect the fluorescence from biotinylated FITC with attomolar sensitivity, thus motivating their application for rapid detection of SARS-CoV-2 using surface-bound S- RBD binding peptide beacons.

3.4 Discussion

In this chapter, adapting the existing technology of TIRF microscope and single-photon sensitive SiPM detector, we fabricated and tested the mini-TIRF that can detect the fluorescent signal from the surface-bound fluorophores from an attomolar solution of fluorophores in 1X PBS, pH 7.4. The device is portable, low-cost, and rapid in (< 30 -minutes). The cartridge costs about \$40, and the read-out box costs about \$300 for assembling a single set of the device (Figure A-8). The cartridge and the read-out box will cost less than \$10, and \$100, respectively, for bulk manufacturing of more than thousands in number. One can use multiple cartridges with a single read-out box, and a single cartridge for once. Hence, the read-out box will be a single-time purchase. Since a single test will consume a single cartridge, we can assume that a single test will cost the price of a single cartridge. Hence, we envision that the integration of peptide beacon candidates from chapter 2 with mini-TIRF, may reduce the LoD of peptide beacons to the attomolar level, thus yielding a rapid,

point-of-care diagnostic platform for SARS-CoV-2.

Our future goal is to immobilize biotinylated peptide beacons on the mini-TIRF and test the performance of the device with S-RBD and real patient samples. Furthermore, we will work toward the fabrication of an integrated on-chip mini-TIRF for evanescent field-assisted detection of surface-bound targets. In addition, using the established pipeline, we will synthesize a library of peptide beacons against respiratory viruses and integrate them with the on-chip mini-TIRF for multiplex detection of the viruses.

3.5 Materials and Methods

3.5.1 Fabrication of Device

The CAD model of the device was constructed using SOLIDWORKS software and Prusa 3D printer was used to print the casings of the device. The streptavidin-coated glass slide was diced into small chips (Length=25 mm and width=10 mm) using die-saw. The diced glass chip was dip-coated with low refractive index polymer (Luvantix ADM PC-340-HA) and UV cured under continuous nitrogen purge. The lower and upper cover was cut out from a 3.175 mm thick opaque acrylic sheet. The visible bandpass filter (530 nm, FWHM 24 nm, $50 \times 50 \text{ mm}^2$) was diced into small pieces using diesaw. A PCB mounted SiPM (KETEK PM3347-WL PIN) was assembled with the 3D printed cartridge along with diced optical filter and lens (Figure A-6) and placed under the sample well keeping them centered to the target TIR spot. A preamplifier (KETEK PEVAL-KIT-MCX) and SiPM bias source (KETEK SIPM-BIAS SOURCE) was used to amplify the SiPM signal. The 3D printed white box contains the preamplifier and bias source. On the top surface of the box, there are slots for the LD and SiPM pins to place the cartridge by plugging the LD pins and SiPMS on the backside of the cartridge into those slots. An opaque lid was used to provide a light-tight environment room during signal readout to avoid background

photons present in the environment (Figure A-8).

3.5.2 Performance of Device

We drop cast a layer of 1 μm fluorescent microspheres (TetraSpeck) on the waveguide from aqueous suspension and placed another drop of the microsphere suspension on the surface-bound microsphere layer and imaged under the confocal microscope. Generally, the objective is moved up in z-direction stepwise during z stack imaging to collect fluorescence signals from different focal planes. Biotin-FITC (ThermoFisher 22030) was serially diluted in 1X PBS, pH 7.4 from nanomolar (nM) to attomolar (aM) concentration. 10 μl droplet of biotinylated FITC in 1X PBS, pH 7.4 was placed in the sample well and incubated for 30 minutes at room temperature. Fluorescence intensity was subsequently measured using a mini-TIRF. The fluorescence data were analyzed and plotted in the Prism software. The limit of detection (LoD) is evaluated from the equation given below:

$$LoD = FI_{Blank} + 3 * SD_{Blank}$$

Where, FI_{Blank} is the fluorescent intensity of the baseline and SD_{Blank} is the standard deviation in the baseline measurement.

3.5.3 Statistics and Reproducibility

All samples were performed in independent quintuplicates (n=5), as indicated. Standard deviation was used to calculate error bars. Statistical analyses were performed using the two-tailed Student's t-test, using the GraphPad software package.

My Contributions

1. Designed and fabricated the device.
2. Characterized the device performance and analyzed the data.

Appendix A

Figures

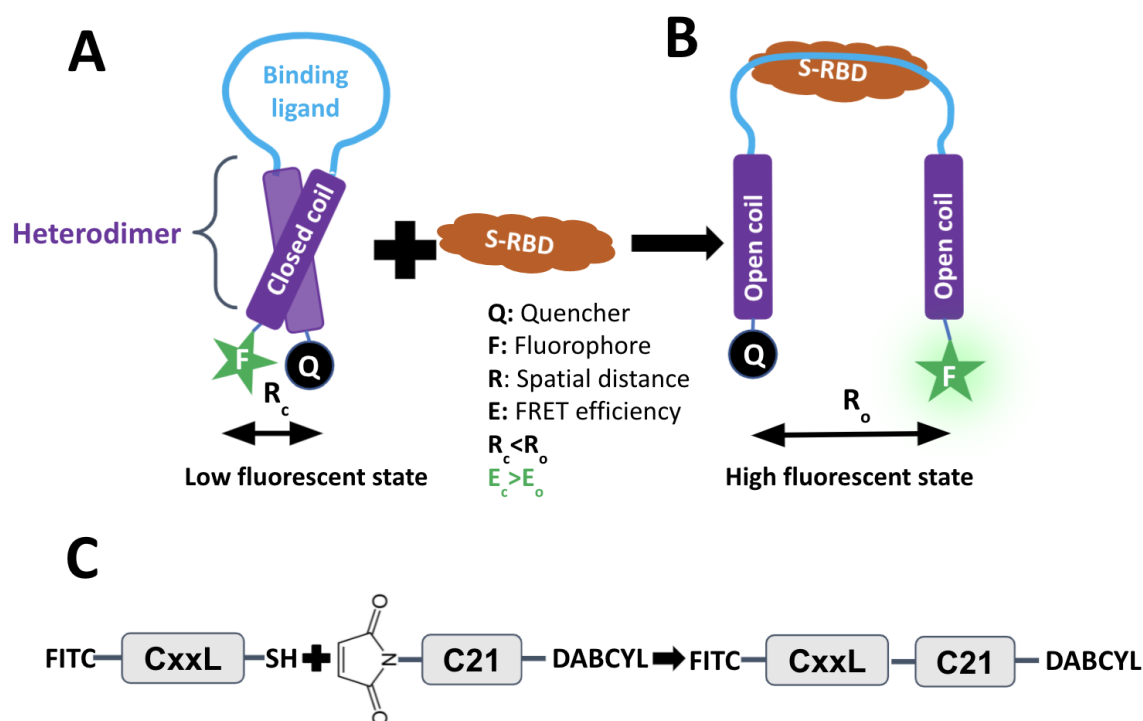


Figure A-1: **Engineering of peptide beacon architecture.** A) Low-fluorescent state is the closed heterodimer state of the peptide beacon in the absence of S-RBD. B) High-fluorescent state is the open-coil state after binding of S-RBD with the loop of the peptide beacon. C) CxxL (25 μ M, 1X PBS, pH 7.4) was added to C21 (25 μ M, 1X PBS, pH 7.4) and incubated at room temperature for 2 hours for the conjugation reaction between the thiol groups of cysteine at the N-terminus of CxxL and the maleimide on the N-terminus of C21.

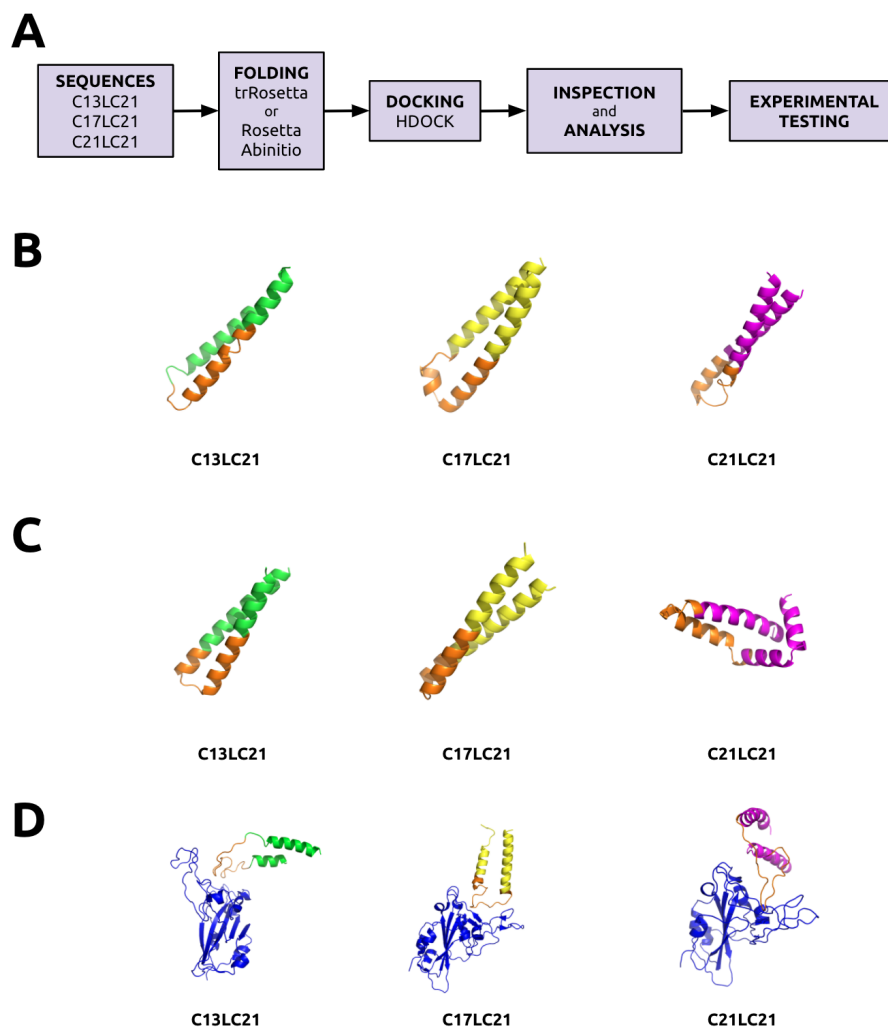


Figure A-2: *In silico* verification of peptide beacon architecture. A) Validation pipeline. Sequences were folded ab initio via trRosetta or Rosetta Abinitio. The top structures were docked to S-RBD via HDOCK. Docked structures were analyzed and candidate beacons were chosen. Highest scoring B) trRosetta structures C) Rosetta Abinitio structures and D) Docked HDOCK structures of the three candidate beacons. The conserved binding peptide moiety is highlighted in orange. S-RBD (derived from PDB 6MOJ) is indicated in blue.

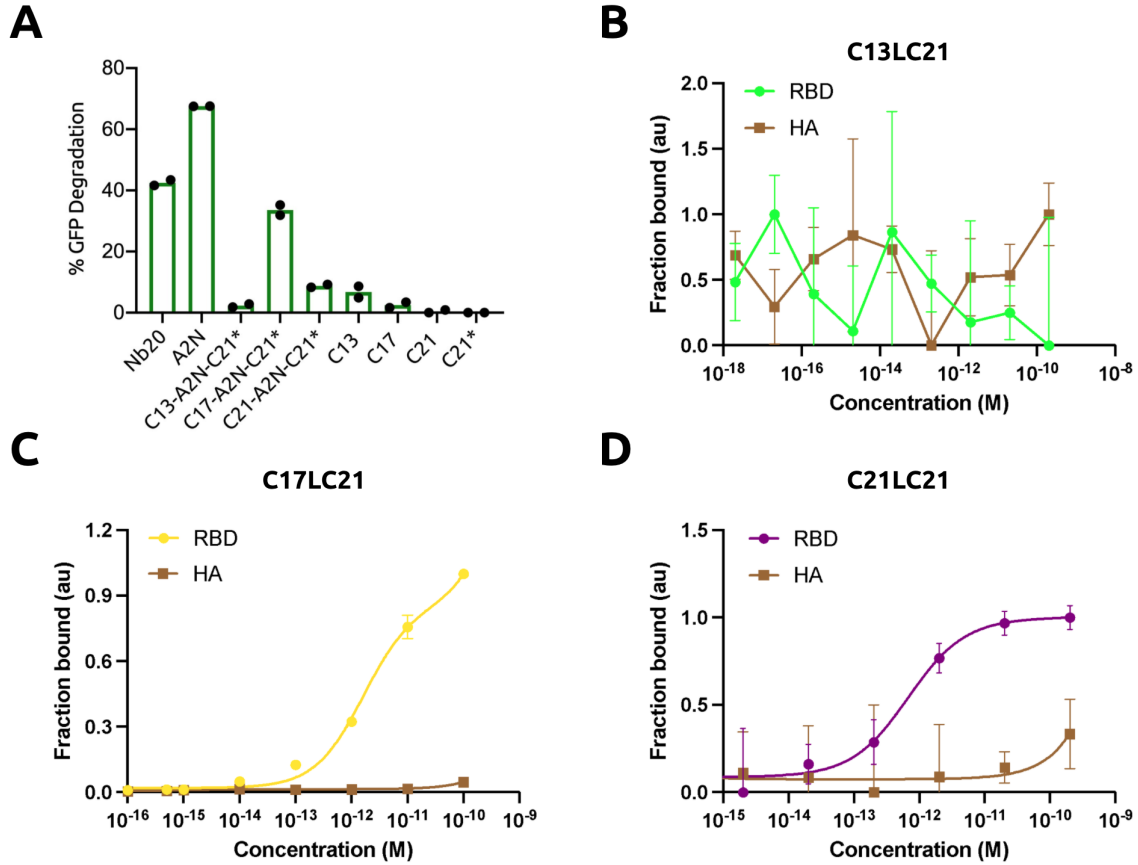


Figure A-3: **Experimental characterization of peptide beacons.** A) Analysis of S-RBD-sfGFP degradation by flow cytometry. All samples were performed in independent transfection duplicates (n=2) and gated on GFP+ fluorescence. Mean percentage of GFP+ cell depletion was calculated in comparison to the S-RBD-sfGFP only control. C13LC21 is referred to as C13-A2N-C21*, C17LC21 is referred to as C17-A2N-C21*, and C21LC21 is referred to as C21-A2N-C21*. Titration of the target recombinant S-RBD and Influenza H3N2 (HA) with 2 nM of HPLC-purified B) C13LC21 (n=3), C) C17LC21 (n=5), D) C21LC21 (n=3) in 1X PBS, pH 7.4.

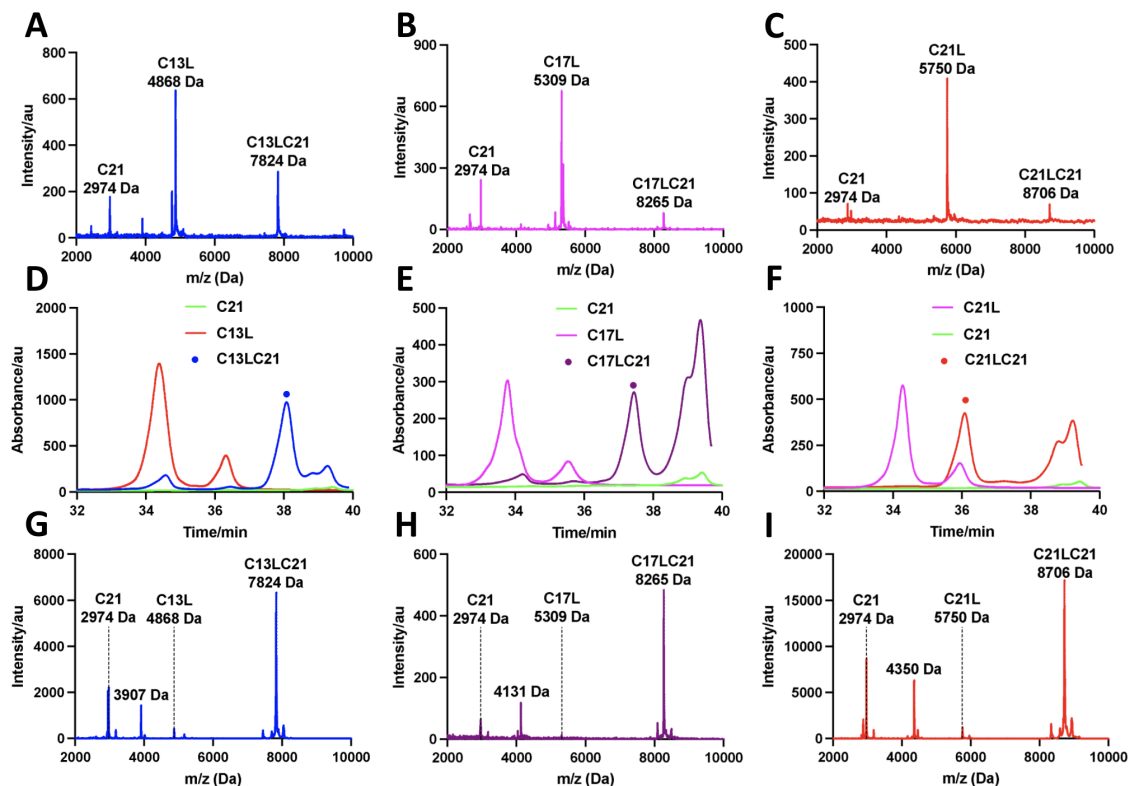


Figure A-4: **Purification and synthesis of peptide beacons.** A-C) MALDI-TOF mass spectrum of CxxL+C21 shows peaks corresponding to C21, CxxL, and CxxLC21. D-F) HPLC chromatograms of CxxLC21, plotted with HPLC chromatograms of CxxL and C21. The chromatogram of C13L+C21, C17L+C21, and C21L+C21 shows the appearance of new peaks having retention times of 38 min, 37 min, and 36 min, respectively (new peaks marked in colored dot in D-E). Fraction of material corresponding to new peaks was collected during HPLC. G-I) MALDI-TOF mass spectrum of collected fraction from HPLC of CxxL+C21 shows dominant peak corresponding to CxxLC21 and negligible peaks corresponding to CxxL and C21. CxxL+C21 represents the reaction mixture of CxxL and C21 after 2 hours of reaction at room temperature. CxxLC21 represents the peptide beacons.

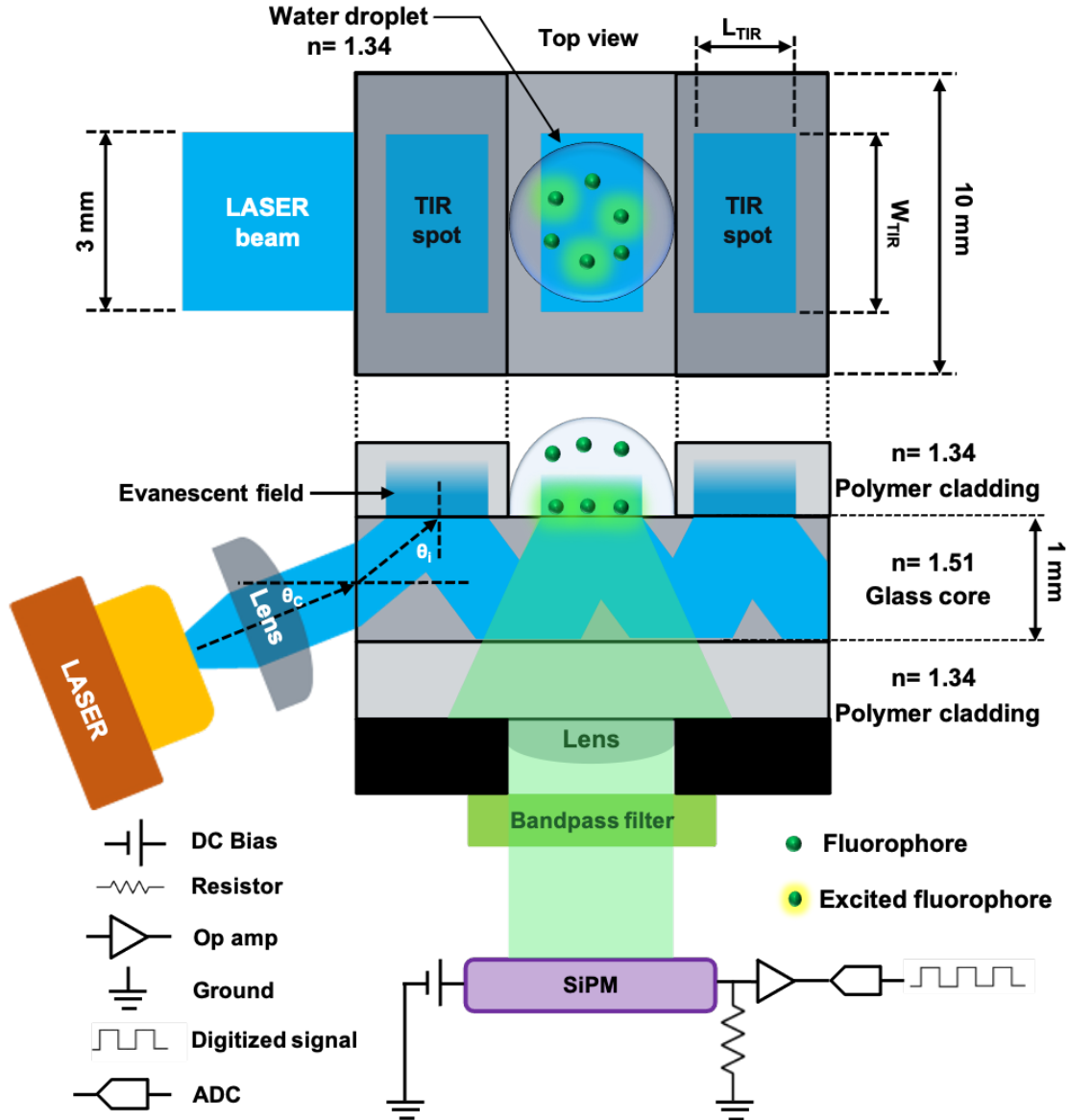


Figure A-5: Design of the mini-TIRF based evanescent-wave fluorescence sensor. The collimated LASER beam hits the side surface of the waveguide at an angle such that the refracted beam within the glass core will hit the core-cladding interface at an angle more than the critical angle of the core-cladding pair. Subsequently, the LASER beam propagates along the length of the waveguide bouncing between the top and bottom core-cladding interface. An optical setup consisting of lens-bandpass filter-SiPM is used to detect the fluorescence emission. The fluorescence signal is quantified through ADC after amplification of the SiPM signal. The top view shows the TIR spots where the laser beam hits the core-cladding interface and creates evanescent waves. L_{TIR} and W_{TIR} are the dimensions of the TIR spot along the length and width of the waveguide.

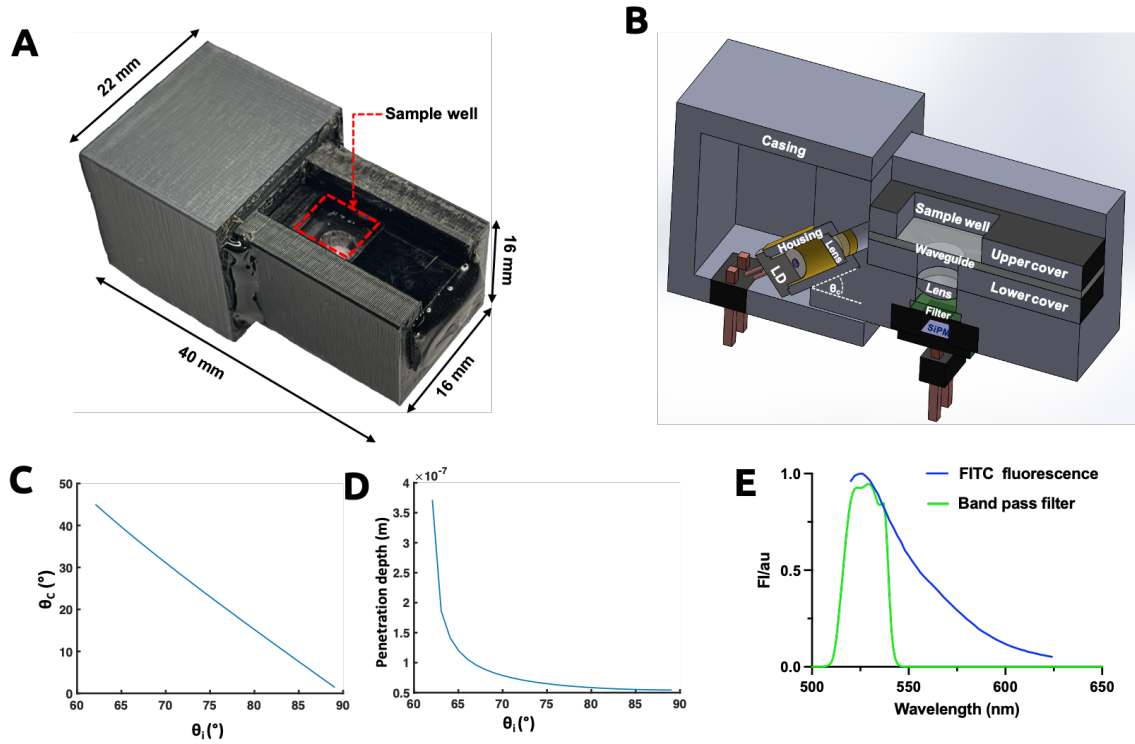


Figure A-6: Design of cartridge. A. 3D printed cartridge. B. The LASER diode (LD) housing holds the LD and collimates the LASER beam. The LD housing is placed at a coupling angle of 38° with the plane of the waveguide. The sample well is parallel and aligned with the lens, filter, and SiPM. C. The graph between angle of incidence that allows TIR and corresponding coupling angles. D. Penetration depths of evanescent field at a different angle of incidence at the core-cladding interface. E. Overlap between bandpass spectrum of the optical filter and emission spectrum of FITC excited at 488 nm.

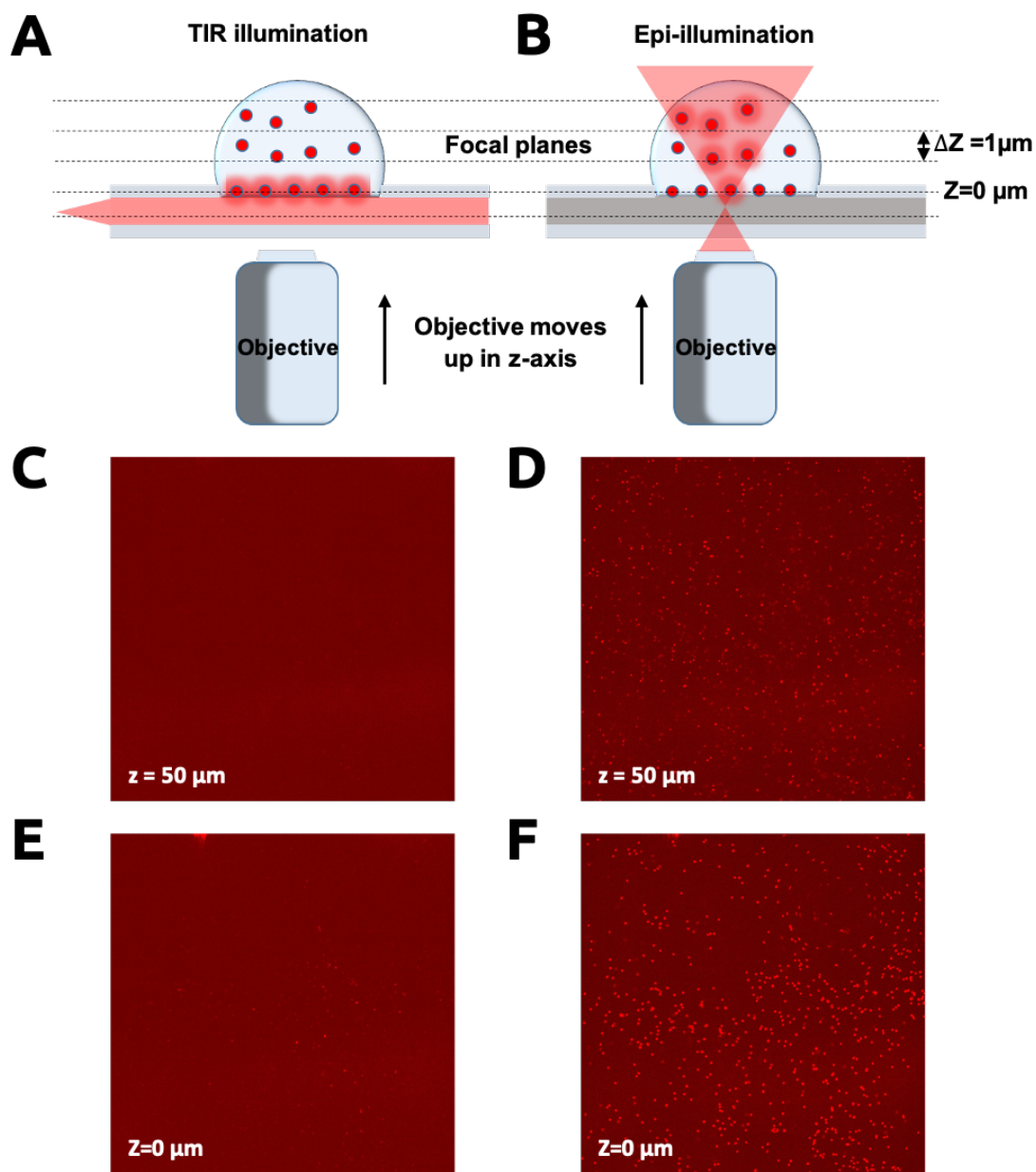


Figure A-7: Confirmation of the presence of evanescent field on mini-TIRF. Z-stack imaging of fluorescent microspheres ($1 \mu\text{m}$) deposited on the glass core within the sample well under A) TIR and B) epi-illumination at $1 \mu\text{m}$ step from surface to $50 \mu\text{m}$ above the surface. C. Focal plane at $50 \mu\text{m}$ above the surface under TIR illumination. D. Focal plane at $50 \mu\text{m}$ above the surface under epi-illumination. E. Focal plane at the surface ($z = 0 \mu\text{m}$) under TIR illumination. F. Focal plane at the surface ($z = 0 \mu\text{m}$) under epi-illumination.

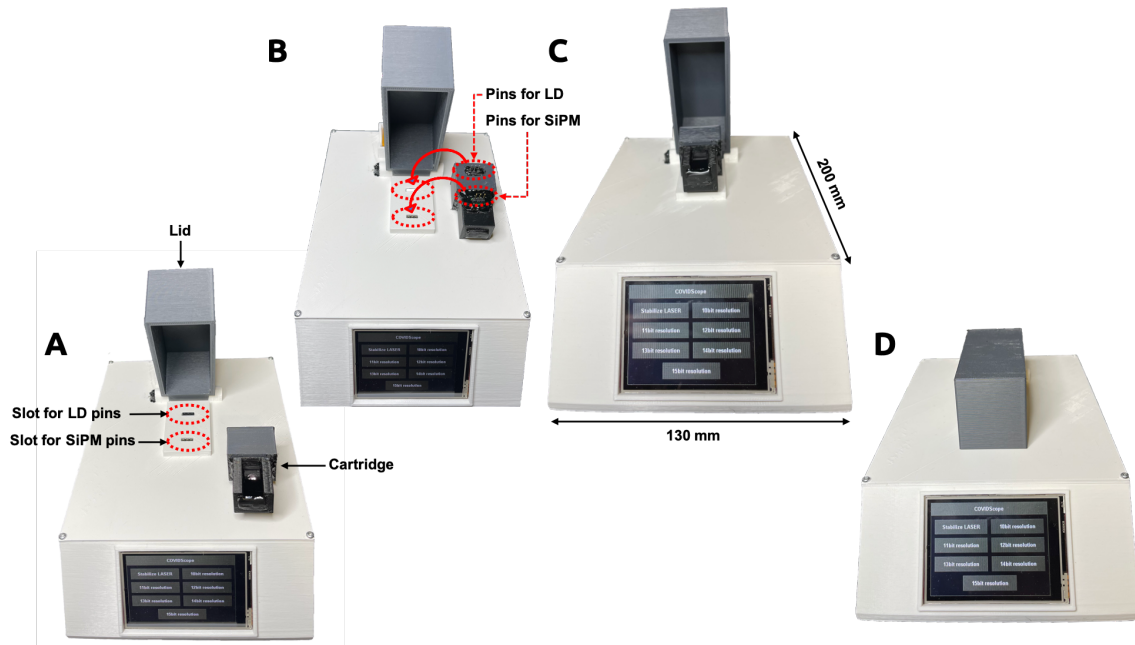


Figure A-8: Fabricated device. A. White box contains the amplification module and Teensy 3.6 development board, along with slots for battery intended for biasing the amplification module. On the top surface of the white box, there are slots for LD pins and SiPM pins. B. LD pins and SiPM pins on the bottom of the cartridge go to the slots on the top surface of the white box. C. The cartridge firmly sits on the box after the LD pins and SiPM pins entering the respective pin slots. D. The lid covers the SiPM to provide a light-tight environment during signal acquisition.

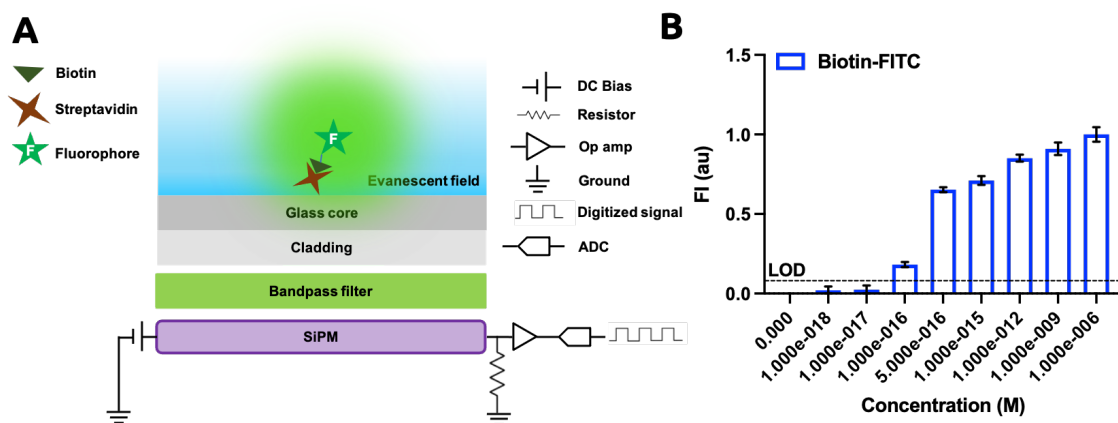


Figure A-9: Detection of biotinylated FITC using mini-TIRF. A. Schematic showing the excitation of biotinylated FITC bound to surface immobilize streptavidin by evanescent field. Bandpass filter selectively allows fluorescent emission and stops stray photons from the scattered evanescent field caused by surface-bound molecules. SiPM detects the photons from the fluorescence emission and an ADC of a microcontroller detects the SiPM signal after amplification. B. Detection of biotinylated FITC in 1X PBS, pH 7.4 from attomolar to micromolar concentration using mini-TIRF. The LoD is defined as the signal more than the baseline signal by thrice of the standard deviation of the baseline signal.

Bibliography

- [1] Ivan Anishchenko, Tamuka M. Chidyausiku, Sergey Ovchinnikov, Samuel J. Pellock, and David Baker. De novo protein design by deep network hallucination. July 2020.
- [2] Praneet C Bala, Benjamin R Eisenreich, Seng Bum Michael Yoo, Benjamin Y Hayden, Hyun Soo Park, and Jan Zimmermann. Openmonkeystudio: Automated markerless pose estimation in freely moving macaques. *BioRxiv*, 2020.
- [3] Lukas Bokelmann, Olaf Nickel, Tomislav Maricic, Svante Pääbo, Matthias Meyer, Stephan Borte, and Stephan Riesenberg. Point-of-care bulk testing for SARS-CoV-2 by combining hybridization capture with improved colorimetric LAMP. *Nature Communications*, 12(1), March 2021.
- [4] Richard Bonneau, Jerry Tsai, Ingo Ruczinski, Dylan Chivian, Carol Rohl, Charlie E. M. Strauss, and David Baker. Rosetta in CASP4: Progress in ab initio protein structure prediction. *Proteins: Structure, Function, and Genetics*, 45(S5):119–126, 2001.
- [5] James P. Broughton, Xianding Deng, Guixia Yu, Clare L. Fasching, Venice Servellita, Jasmeet Singh, Xin Miao, Jessica A. Streithorst, Andrea Granados, Alicia Sotomayor-Gonzalez, Kelsey Zorn, Allan Gopez, Elaine Hsu, Wei Gu, Steve Miller, Chao-Yang Pan, Hugo Guevara, Debra A. Wadford, Janice S. Chen, and Charles Y. Chiu. CRISPR–cas12-based detection of SARS-CoV-2. *Nat Biotechnol*, 38(7):870–874, apr 2020.
- [6] Stephen A. Bustin and Tania Nolan. RT-qPCR testing of SARS-CoV-2: A primer. *International Journal of Molecular Sciences*, 21(8):3004, April 2020.
- [7] Ho-Man Chan, Lai-Sheung Chan, Ricky Ngok-Shun Wong, and Hung-Wing Li. Direct quantification of single-molecules of microrna by total internal reflection fluorescence microscopy. *Analytical chemistry*, 82(16):6911–6918, 2010.
- [8] Pranam Chatterjee, Manvitha Ponnappati, Christian Kramme, Alexandru M. Plesa, George M. Church, and Joseph M. Jacobson. Targeted intracellular degradation of SARS-CoV-2 via computationally optimized peptide fusions. *Communications Biology*, 3(1), November 2020.

- [9] Victor M Corman, Verena Claudia Haage, Tobias Bleicker, Marie Luisa Schmidt, Barbara Mühlemann, Marta Zuchowski, Wendy K Jo, Patricia Tscheak, Elisabeth Möncke-Buchner, Marcel A Müller, Andi Krumbholz, Jan Felix Drexler, and Christian Drosten. Comparison of seven commercial SARS-CoV-2 rapid point-of-care antigen tests: a single-centre laboratory evaluation study. *The Lancet Microbe*, April 2021.
- [10] Xiong Ding, Kun Yin, Ziyue Li, Rajesh V. Lalla, Enrique Ballesteros, Maroun M. Sfeir, and Changchun Liu. Ultrasensitive and visual detection of SARS-CoV-2 using all-in-one dual CRISPR-cas12a assay. *Nature Communications*, 11(1), September 2020.
- [11] Lu Guo, Xuehan Sun, Xinge Wang, Chen Liang, Haiping Jiang, Qingqin Gao, Moyu Dai, Bin Qu, Sen Fang, Yihuan Mao, Yangcan Chen, Guihai Feng, Qi Gu, Ruiqi Rachel Wang, Qi Zhou, and Wei Li. SARS-CoV-2 detection with CRISPR diagnostics. *Cell Discov*, 6(1), may 2020.
- [12] See-Lok Ho, Ho-Man Chan, Amber Wai-Yan Ha, Ricky Ngok-Shun Wong, and Hung-Wing Li. Direct quantification of circulating mirnas in different stages of nasopharyngeal cancerous serum samples in single molecule level with total internal reflection fluorescence microscopy. *Analytical chemistry*, 86(19):9880–9886, 2014.
- [13] Seok-Jin Jeong, Sang-Kyu Park, Jun-Keun Chang, and Seong-Ho Kang. Ultra-sensitive real-time single-dna molecules detection at a fused-silica/water interface using tirmf technique. *Bulletin of the Korean Chemical Society*, 26(6):979–982, 2005.
- [14] Seong Ho Kang, Michael R Shortreed, and Edward S Yeung. Real-time dynamics of single-dna molecules undergoing adsorption and desorption at liquid- solid interfaces. *Analytical chemistry*, 73(6):1091–1099, 2001.
- [15] Max J. Kellner, Jeremy G. Koob, Jonathan S. Gootenberg, Omar O. Abudayyeh, and Feng Zhang. SHERLOCK: nucleic acid detection with CRISPR nucleases. *Nature Protocols*, 14(10):2986–3012, September 2019.
- [16] Bhavesh D. Kevadiya, Jatin Machhi, Jonathan Herskovitz, Maxim D. Oleynikov, Wilson R. Blomberg, Neha Bajwa, Dhruvkumar Soni, Srijanee Das, Mahmudul Hasan, Milankumar Patel, Ahmed M. Senan, Santhi Gorantla, JoEllyn McMillan, Benson Edagwa, Robert Eisenberg, Channabasavaiah B. Gurumurthy, St Patrick M. Reid, Chamindie Punyadeera, Linda Chang, and Howard E. Gendelman. Diagnostics for SARS-CoV-2 infections. *Nature Materials*, 20(5):593–605, February 2021.
- [17] Fang Luo, Gege Qin, Tie Xia, and Xiaohong Fang. Single-molecule imaging of protein interactions and dynamics. *Annual Review of Analytical Chemistry*, 13:337–361, 2020.

- [18] Lena Mautner, Christin-Kirsty Baillie, Heike Marie Herold, Wolfram Volkwein, Patrick Guertler, Ute Eberle, Nikolaus Ackermann, Andreas Sing, Melanie Pavlovic, Ottmar Goerlich, Ulrich Busch, Lars Wassill, Ingrid Huber, and Armin Baiker. Rapid point-of-care detection of SARS-CoV-2 using reverse transcription loop-mediated isothermal amplification (RT-LAMP). *Virology Journal*, 17(1), October 2020.
- [19] Yukihiro Miyanaga, Satomi Matsuoka, and Masahiro Ueda. Single-molecule imaging techniques to visualize chemotactic signaling events on the membrane of living dictyostelium cells. In *Chemotaxis*, pages 417–435. Springer, 2009.
- [20] Carolin Mueller and Tom N. Grossmann. Coiled-coil peptide beacon: A tunable conformational switch for protein detection. *Angewandte Chemie International Edition*, 57(52):17079–17083, November 2018.
- [21] Martin Oheim, Adi Salomon, Adam Weissman, Maia Brunstein, and Ute Becherer. Calibrating evanescent-wave penetration depths for biological TIRF microscopy. *Biophysical Journal*, 117(5):795–809, September 2019.
- [22] Maturada Patchsung, Krittapas Jantarug, Archiraya Pattama, Kanokpol Aphicho, Surased Suraritdechachai, Piyachat Meesawat, Khomkrit Sappakhaw, Natawat Leelahakorn, Theerawat Ruenkam, Thanakrit Wongsatit, Niracha Athipanyasilp, Bhumrapee Eiamthong, Benya Lakkanasirorat, Thitima Phoodokmai, Nootaree Niljianskul, Danaya Pakotiprapha, Sittinan Chanarat, Aimorn Homchan, Ruchanok Tinikul, Philaiwarong Kamutira, Kochakorn Phiwkaow, Sahachat Soithongcharoen, Chadaporn Kantiwiriyanitch, Vinutsada Pongsupasa, Duangthip Trisrivirat, Juthamas Jaroensuk, Thanyaporn Wongnate, Somchart Maenpuen, Pimchai Chaiyen, Sirichai Kamnerdnakta, Jirawat Swangsri, Suebwong Chuthapisith, Yongyut Sirivatanauksorn, Chutikarn Chaimayo, Ruengpung Sutthent, Wannee Kantakamalakul, Julia Joung, Alim Ladha, Xin Jin, Jonathan S. Gootenberg, Omar O. Abudayyeh, Feng Zhang, Navin Horthongkham, and Chayasith Uttamapinant. Clinical validation of a cas13-based assay for the detection of SARS-CoV-2 RNA. *Nat Biomed Eng*, 4(12):1140–1149, aug 2020.
- [23] Samara L Reck-Peterson, Nathan D Derr, and Nico Stuurman. Imaging single molecules using total internal reflection fluorescence microscopy (tirfm). *Cold Spring Harbor Protocols*, 2010(3):pdb-top73, 2010.
- [24] Charles J. Russell, Meng Hu, and Faten A. Okda. Influenza hemagglutinin protein stability, activation, and pandemic risk. *Trends in Microbiology*, 26(10):841–853, October 2018.
- [25] Benjamin R Schudel, Melikhan Tanyeri, Arnab Mukherjee, Charles M Schroeder, and Paul JA Kenis. Multiplexed detection of nucleic acids in a combinatorial screening chip. *Lab on a Chip*, 11(11):1916–1923, 2011.

- [26] Franziska Thomas, Aimee L. Boyle, Antony J. Burton, and Derek N. Woolfson. A set of de Novo Designed parallel heterodimeric coiled coils with quantified dissociation constants in the micromolar to sub-nanomolar regime. *Journal of the American Chemical Society*, 135(13):5161–5166, March 2013.
- [27] Makio Tokunaga, Kazuo Kitamura, Kiwamu Saito, Atsuko Hikikoshi Iwane, and Toshio Yanagida. Single molecule imaging of fluorophores and enzymatic reactions achieved by objective-type total internal reflection fluorescence microscopy. *Biochemical and biophysical research communications*, 235(1):47–53, 1997.
- [28] Wenling Wang, Yanli Xu, Ruqin Gao, Roujian Lu, Kai Han, Guizhen Wu, and Wenjie Tan. Detection of SARS-CoV-2 in different types of clinical specimens. *JAMA*, March 2020.
- [29] Tetsuichi Wazawa and Masahiro Ueda. Total internal reflection fluorescence microscopy in single molecule nanobioscience. In *Microscopy Techniques*, pages 77–106. Springer Berlin Heidelberg, May 2005.
- [30] Tetsuichi Wazawa and Masahiro Ueda. Total internal reflection fluorescence microscopy in single molecule nanobioscience. *Microscopy Techniques*, pages 77–106, 2005.
- [31] Yufei Xiang, Sham Nambulli, Zhengyun Xiao, Heng Liu, Zhe Sang, W. Paul Duprex, Dina Schneidman-Duhovny, Cheng Zhang, and Yi Shi. Versatile and multivalent nanobodies efficiently neutralize SARS-CoV-2. *Science*, page eabe4747, November 2020.
- [32] Guanhua Xun, Stephan Thomas Lane, Vassily Andrew Petrov, Brandon Elliott Pepa, and Huimin Zhao. A rapid, accurate, scalable, and portable testing system for COVID-19 diagnosis. *Nature Communications*, 12(1), May 2021.
- [33] Yumeng Yan, Huanyu Tao, Jiahua He, and Sheng-You Huang. The HDock server for integrated protein–protein docking. *Nature Protocols*, 15(5):1829–1852, April 2020.
- [34] Jianyi Yang, Ivan Anishchenko, Hahnbeom Park, Zhenling Peng, Sergey Ovchinnikov, and David Baker. Improved protein structure prediction using predicted interresidue orientations. *Proceedings of the National Academy of Sciences*, 117(3):1496–1503, January 2020.
- [35] Gang Yao, Xiaohong Fang, Hiroaki Yokota, Toshio Yanagida, and Weihong Tan. Monitoring molecular beacon dna probe hybridization at the single-molecule level. *Chemistry—A European Journal*, 9(22):5686–5692, 2003.